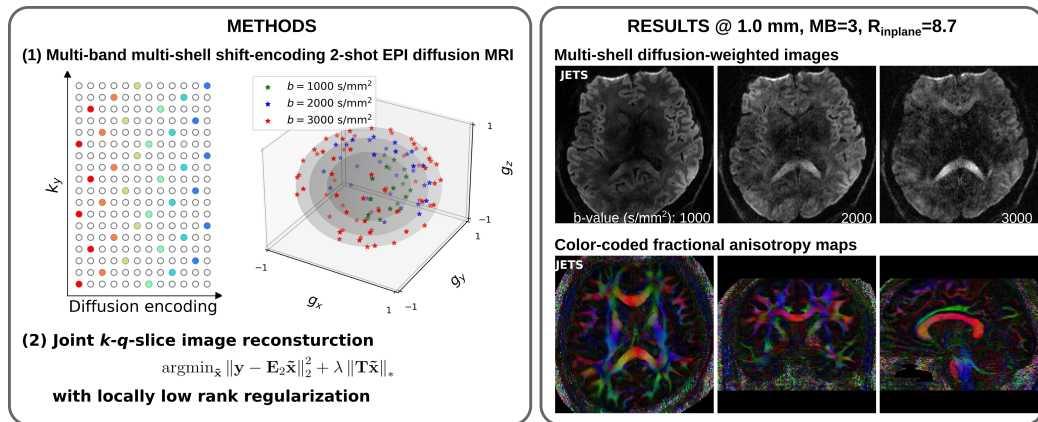


Graphical Abstract

Accelerated Diffusion Magnetic Resonance Imaging at 7 T: Joint Reconstruction for Multi-Shell Multi-Band Shift-Encoded Echo Planar Imaging (JETS-EPI)

Zhengguo Tan, Patrick Alexander Liebig, Robin Martin Heidemann, Frederik Bernd Laun, Florian Knoll



Highlights

Accelerated Diffusion Magnetic Resonance Imaging at 7 T: Joint Reconstruction for Multi-Shell Multi-Band Shift-Encoded Echo Planar Imaging (JETS-EPI)

Zhengguo Tan, Patrick Alexander Liebig, Robin Martin Heidemann, Frederik Bernd Laun, Florian Knoll

- Novel accelerated diffusion acquisition with shifted phase encoding among diffusion directions for complementary k - q -space sampling at 7 T
- Generalized joint k - q -slice diffusion-weighted image reconstruction with overlapping locally low-rank regularization
- 5 min 1.2 mm isotropic resolution with b -value 1000 s/mm^2 and 32 diffusion directions for in vivo whole-brain diffusion tensor imaging
- 23 min 1 mm isotropic resolution with three-shell high b -values (up to 3000 s/mm^2) and 126 diffusion directions for in vivo whole-brain diffusion tensor imaging and fiber orientation distribution function (fODF) mapping

Accelerated Diffusion Magnetic Resonance Imaging at 7 T: Joint Reconstruction for Multi-Shell Multi-Band Shift-Encoded Echo Planar Imaging (JETS-EPI)

Zhengguo Tan^a, Patrick Alexander Liebig^b, Robin Martin Heidemann^b,
Frederik Bernd Laun^c, Florian Knoll^a

^a*Department Artificial Intelligence in Biomedical Engineering (AIBE),
Friedrich-Alexander-Universität Erlangen-Nürnberg, Erlangen, Germany*

^b*Siemens Healthcare GmbH, Erlangen, Germany*

^c*Institute of Radiology, University Hospital Erlangen, Friedrich-Alexander-Universität
Erlangen-Nürnberg, Erlangen, Germany*

Abstract

The pursuit of high spatial-angular-temporal resolution for in vivo diffusion-weighted magnetic resonance imaging (DW-MRI) at ultra-high field strength (e.g., 7 T) is important in understanding brain microstructure and function. Such pursuit, however, faces several technical challenges. First, increased off-resonance and shorter T_2 relaxation require faster echo train readouts. Second, high angular resolution in q -space requires the use of high and/or multiple b -values, which increases noise in diffusion-weighted images and prolongs scan time. Multi-shot interleaved echo-planar imaging (EPI) and advanced reconstruction strategies, e.g., multiplexed sensitivity-encoding (MUSE) and compressed sensing with structured low-rank matrix completion (MUSSELS), have been proven suitable for high-resolution DW-MRI. These methods, however, do not explore complementary k - q -space sampling and require longer scan time compared to single-shot EPI. To address these challenges, we developed a novel joint reconstruction for multi-shell multi-

band shift-encoding acquisition at 7 T (JETS-EPI). In comparison to MUSE and MUSSELS, it allows for faster acquisition with the use of high inplane acceleration and only two shots per diffusion direction. Moreover, the proposed joint reconstruction exhibits better denoising of DW images and clearer delineation of fiber distributions.

Keywords: Diffusion-weighted magnetic resonance imaging, Echo planar imaging, Ultra high field, Joint reconstruction, Low rank, Simultaneous multi slice

¹ **1. Introduction**

² Diffusion-weighted magnetic resonance imaging (DW-MRI) ([Le Bihan et al., 1986; Merboldt et al., 1985](#)) is a non-invasive modality that is sen-
³ sitive to Brownian motion of water molecules. DW-MRI forms the basis for
⁴ diffusion tensor imaging (DTI) ([Basser et al., 1994; Mori et al., 1999](#)) and
⁵ high angular resolution diffusion imaging (HARDI) ([Tuch et al., 2002](#)), and
⁶ has been widely used in acute brain ischemia diagnosis, in tumor detection
⁷ and staging, and in neuroscience ([Jones, 2010](#)).

⁹ For DW-MRI acquisition, the commonly used pulse sequence is single-
¹⁰ shot echo-planar imaging (SS-EPI) ([Mansfield, 1977](#)). SS-EPI is capable
¹¹ of rapidly acquiring one DW image per radio-frequency excitation at the
¹² order of 100 milliseconds, and is thus motion robust. However, conventional
¹³ SS-EPI, even with three-fold accelerated acquisition ([Bammer et al., 2001](#))
¹⁴ using parallel imaging ([Roemer et al., 1990; Ra and Rim, 1993; Pruessmann et al., 1999; Griswold et al., 2002](#)), still suffers from low spatial resolution
¹⁵ and geometric distortions.

¹⁷ In the quest for high-spatial-angular-resolution and minimal-geometry-
¹⁸ distortion DW-MRI, tremendous efforts have been made. Instead of SS-EPI,
¹⁹ advanced pulse sequences based on multi-shot EPI have been developed, in-
²⁰ cluding but not limited to interleaved EPI ([Butts et al., 1993](#)), PROPELLER
²¹ ([Pipe et al., 2002](#)), readout-segmented EPI ([Porter and Heidemann, 2009; Heidemann et al., 2010](#)), and spiral ([Truong and Guidon, 2014](#)). Multi-shot
²³ EPI acquisition, however, requires not only longer scan time, but also shot-to-
²⁴ shot phase variation correction (due to the use of motion-sensitive diffusion
²⁵ gradients).

26 The standard shot-to-shot phase variation correction acquires navigator
27 echoes at the cost of increased acquisition time. To eliminate this, advanced
28 self-navigated image reconstruction techniques have been developed. Multi-
29 plexed sensitivity encoding (MUSE) based on simultaneous-multi-slice (SMS)
30 (Maudsley, 1980; Breuer et al., 2005) 4-shot interleaved EPI achieved DW-
31 MRI with sub-millimeter inplane resolution and maximal b -value 2000 s/mm^2
32 at 3 T (Chen et al., 2013). In MUSE, four shots (i.e., four-fold acceleration
33 per shot) are needed because of two reasons. First, high spatial resolution
34 requires the use of multi-shot acquisition, which employs shorter echo train
35 length per shot. This allows for reduced echo time and less spatial distor-
36 tion. Second, MUSE employs parallel imaging (e.g. SENSE) to reconstruct
37 shot images for the extraction of shot-to-shot phase variation, and four-fold
38 acceleration per shot is achievable in parallel imaging.

39 Beyond parallel imaging, compressed sensing opens up the possibility of
40 higher acceleration in MRI (Lustig et al., 2007; Block et al., 2007). Multi-shot
41 reconstruction techniques based on structured low-rank matrix completion
42 (MUSSELS) (Mani et al., 2017; Bilgic et al., 2019) achieved 5-shot DW-
43 MRI with 9-fold acceleration per shot. Recently, joint usage of structured
44 low-rank constraints and explicit phase mapping (JULEP) (Dai et al., 2023)
45 incorporated iterative phase update into MUSSELS using 4-shot DW-MRI
46 with 4-fold acceleration per shot. All these techniques target the recon-
47 struction of one DW image from interleaved EPI using at least 4 shots, i.e.,
48 joint- k - q -space acceleration is not explored.

49 Joint- k - q -space acceleration can be achieved via proper regularization
50 along the diffusion encoding direction. Relevant examples are diffusion ac-

celeration with Gaussian process estimated reconstruction (DAGER) (Wu et al., 2019) and magnitude-based spatial-angular locally low-rank regularization (SPA-LLR) (Hu et al., 2020). DAGER and SPA-LLR address the reconstruction problem of single-shell diffusion data with b -values of 1000 and 2000 s/mm², respectively. However, DAGER requires many diffusion directions, whereas SPA-LLR employs the standard interleaved EPI acquisition (i.e., all DW acquisition shares the same inplane sampling pattern). Consequently, these techniques still require long acquisition time.

In this work, we propose a Joint k - q -slice rEconsTruction framework for multi-band multi-shell Shift-encoded EPI at 7T (dubbed as JETS-EPI). First, our acquisition method differs from most existing techniques as it shifts the k -space in-plane sampling pattern along the phase encoding (k_y) direction. This shifting creates complementary k - q -space sampling. Second, our reconstruction framework generalizes to jointly reconstruct multi-slice multi-shell multi-direction DW images. This is built upon comprehensive modeling of the acquisition process and construction of regularization terms (e.g. LLR) as proximal operators. We compared our proposed method with state-of-the-art multi-shot reconstruction techniques, i.e., MUSE and MUS-SELS, as well as the established DW image denoising algorithm, i.e., local PCA (Manjón et al., 2013; Veraart et al., 2016). Our proposed method achieves 7T three-shell high b -value (up to 3000 s/mm²) and 126 diffusion direction measurements at 1 mm isotropic resolution in less than 23 min.

⁷³ **2. Material and methods**

⁷⁴ *2.1. Multi-band multi-shell shift-encoded EPI acquisition*

⁷⁵ Fig. 1 (A) displays diffusion weighted image acquisition based on two-
⁷⁶ shot interleaved EPI. Conventionally, such a sampling pattern is repeated
⁷⁷ for all diffusion directions. In contrast, we propose the k_y -shifted diffusion
⁷⁸ encoding, as shown in Fig. 1 (B). The interleaved EPI sampling pattern is
⁷⁹ shifted by one k_y line per diffusion direction, with the cycling period being
⁸⁰ the in-plane acceleration factor. Fig. 1 (C) displays the employed multi-shell
⁸¹ sampling pattern. Every diffusion direction is distinct from others, thereby
⁸² constructing a non-colinear sampling pattern. This k_y -shifted non-colinear
⁸³ diffusion encoding exploits complementary k - q -space sampling. Its benefits
⁸⁴ are two-fold. First, the k_y -shifting is linear and retains consistent echo spac-
⁸⁵ ing. Second, DW images share anatomical structures but differ in image
⁸⁶ contrast depending on b -values and diffusion directions, thus complementary
⁸⁷ q -space sampling is well suited for the exploration of structural similarity.

⁸⁸ *2.2. In vivo acquisition protocols*

⁸⁹ We implemented multiple in-vivo acquisition protocols at a clinical 7T
⁹⁰ MR system (MAGNETOM Terra, Siemens Healthineers, Erlangen, Ger-
⁹¹ many) equipped with a 32-channel head coil (Nova Medical, Wilmington,
⁹² MA, USA) and the XR-gradient system (80 mT/m @ 200 T/m/s). To cali-
⁹³ brate coil sensitivity maps, reference scans employed a gradient-echo (GRE)
⁹⁴ sequence. Spectral fat saturation and mono-polar diffusion-encoding gradi-
⁹⁵ ents were used. The phase-encoding direction was selected as anterior-to-
⁹⁶ posterior.

97 This study was approved by the local ethics committee, and informed con-
98 sent was obtained before scanning healthy volunteers. Detailed acquisition
99 parameters are listed below.

100 *2.2.1. Single-shell diffusion acquisition at 1.2 mm isotropic resolution*

101 This protocol employed 220 mm FOV in both read and phase-encoding di-
102 rections, base resolution 182, 94 slices, bandwidth 1832 Hz/Pixel, echo spac-
103 ing 0.75 ms, TE 47 ms, TR 4300 ms, 2 shots per diffusion direction, in-plane
104 acceleration 3 as well as partial Fourier 6/8 along the phase-encoding direc-
105 tion, and multi-band factor 2. This results in 8.7×2 fold acceleration per
106 shot. 30 diffusion directions with b -value 1000 s/mm^2 and 2 diffusion direc-
107 tions with b -value 50 s/mm^2 were acquired at a total scan time of $5'3''$. Given
108 the high spatial resolution and the short scan time, this protocol fits well into
109 clinical studies.

110 *2.2.2. Three-shell diffusion acquisition at 1 mm isotropic resolution*

111 This protocol employed the same FOV, shots, inplane acceleration, and
112 partial Fourier as Section 2.2.1. Other parameters were base resolution 214,
113 114 slices, bandwidth 1460 Hz/Pixel, echo spacing 0.81 ms, TE 66 ms, TR
114 5200 ms, and multi-band factor 3. This results in 8.7×3 fold acceleration
115 per shot. As shown in Fig. 1 (C), three shells were sampled (1st shell: 20 dif-
116 fusion directions with b -value 1000 s/mm^2 , 2nd shell: 30 diffusion directions
117 with b -value 2000 s/mm^2 , and 3rd shell: 64 diffusion directions with b -value
118 3000 s/mm^2). b_0 acquisition was interspersed every ten diffusion directions.
119 This corresponds to a total of 126 DW acquisition and $22'25''$ scan time.
120 This protocol demonstrates the capabilities of JETS-EPI in achieving high

₁₂₁ spatial-angular-temporal resolution.

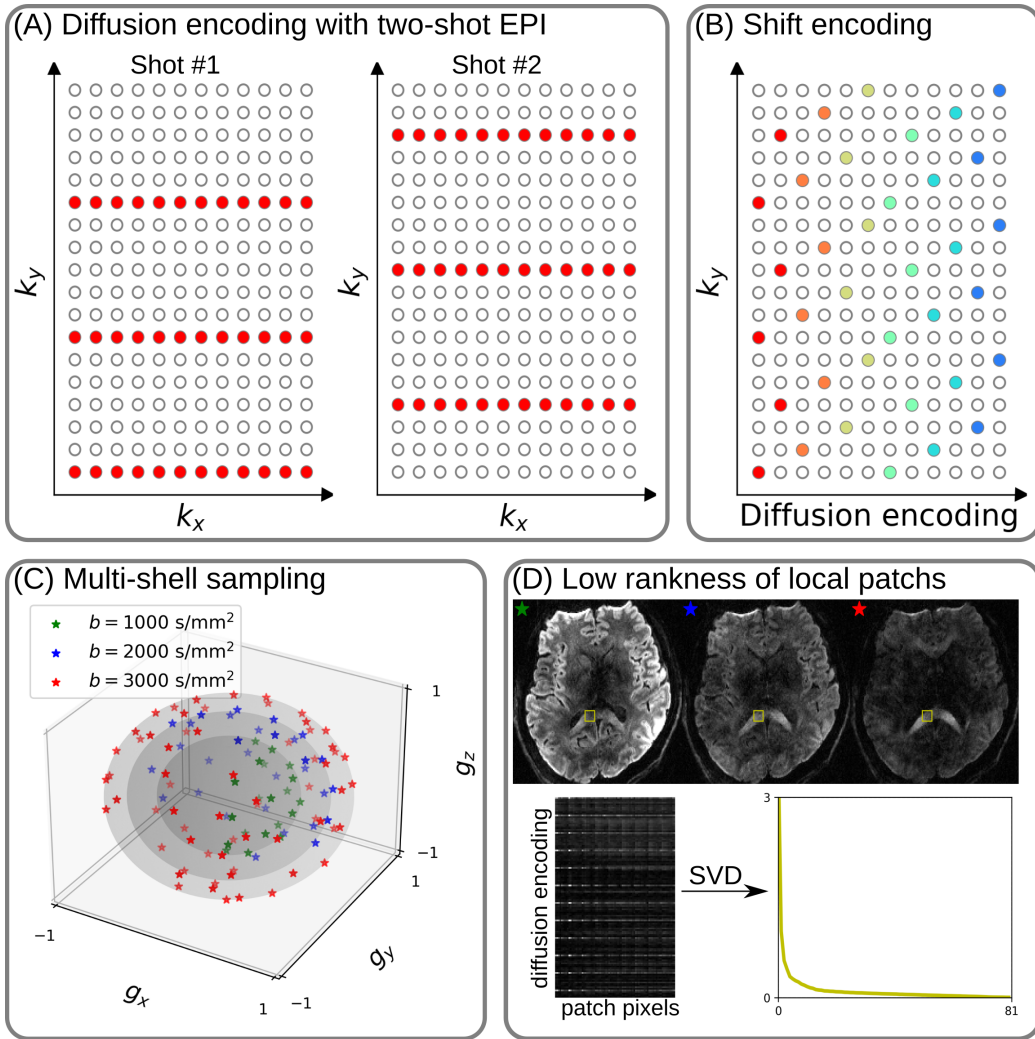


Figure 1: (A) An example DW-MRI acquisition with two-shot interleaved EPI acquisition. (B) The proposed k_y shifted diffusion encoding scheme. This example employs two shots per DW image. Therefore, every two columns have the same color. (C) An example multi-shell sampling scheme. (D) Low rankness of local image patches (as extracted from the yellow blocks) along multi-shell diffusion encoding.

122 2.3. Forward modeling

123 Our proposed acquisition method yields multi-dimensional but slice col-
124 lapsed k -space data $\mathbf{y}_{c,q,s}$, where c, q, s denotes the index of the coil sensitivity
125 map, the diffusion encoding, and the shot, respectively. Such acquisition can
126 be modeled in two ways.

First, the acquired k -space data \mathbf{y} is mapped from individual shot images $\mathbf{x}_{q,s,z}$ via the forward model,

$$\mathbf{y}_{c,q,s} = \mathbf{P}_{q,s} \boldsymbol{\Sigma} \boldsymbol{\Theta}_z \mathbf{F} \mathbf{S}_c \mathbf{x}_{q,s,z} \quad (1)$$

$$\mathbf{y} := \mathbf{E}_1 \mathbf{x} \quad (2)$$

127 Here, the encoding matrix \mathbf{E}_1 comprises a chain of linear operators. Every
128 shot image \mathbf{x} is point-wise multiplied by a set of coil sensitivity maps (\mathbf{S}) and
129 Fourier transformed (\mathbf{F}). The output is then point-wise multiplied by the
130 multi-slice phase map ($\boldsymbol{\Theta}$) with z the slice index in simultaneously excited
131 slices. This operator shifts individual slice along the phase-encoding direction
132 via varying phase modulation (Breuer et al., 2005). The SMS k -space data
133 is then summed (collapsed, $\boldsymbol{\Sigma}$) along the slice dimension and masked (point-
134 wise multiplied, \mathbf{P}) by the sampling pattern at every diffusion encoding and
135 shot.

136 Second, for diffusion MRI based on multi-shot EPI, shot images per dif-
137 fusion encoding need to be combined as one DW image ($\tilde{\mathbf{x}}$). One method is
138 to perform magnitude average (Chen et al., 2013) or root-sum-squares (RSS)
139 (Mani et al., 2017) of shot images. This method is robust to motion, but
140 sub-optimal with respect to signal-to-noise ratio (SNR) (Guhaniyogi et al.,
141 2016). Alternatively, shot combination is done via shot-to-shot phase vari-
142 ation correction (Liu et al., 2005; Chen et al., 2013). This method can be

₁₄₃ written as point-wise multiplication between the shot-to-shot phase variation
₁₄₄ (Φ) and the DW image ($\tilde{\mathbf{x}}$),

$$\mathbf{x}_{q,s,z} = \Phi_{q,s,z} \tilde{\mathbf{x}}_{q,z} \quad (3)$$

₁₄₅ Note that $\tilde{\mathbf{x}}$ can be obtained by applying the adjoint of Φ to \mathbf{x} . In MUSE,
₁₄₆ Φ is obtained by parallel imaging reconstruction of all shots with subsequent
₁₄₇ phase smoothing of every shot image (e.g. Hanning window). Based on this
₁₄₈ phase correction method, the complete forward model follows

$$\mathbf{y} := \mathbf{E}_2 \tilde{\mathbf{x}} = \mathbf{E}_1 \Phi \tilde{\mathbf{x}} \quad (4)$$

₁₄₉ where the encoding matrix \mathbf{E}_2 comprises the chain of the shot-to-shot phase
₁₅₀ variation Φ and the encoding matrix \mathbf{E}_1 .

₁₅₁ We implemented these two encoding matrices in SigPy ([Ong and Lustig, 2019](#)), utilizing the concept of object-oriented linear operator abstraction.

₁₅₃ 2.4. Joint k - q -slice reconstruction

₁₅₄ Based on the generalized forward models in Eqs. (2) and (4), our proposed
₁₅₅ joint k - q -slice reconstruction can be formulated as a three-step approach.

₁₅₆ I. Joint reconstruction of all shot images by solving the following inverse
₁₅₇ problem with the LLR regularization:

$$\operatorname{argmin}_{\mathbf{x}} \|\mathbf{y} - \mathbf{E}_1 \mathbf{x}\|_2^2 + \lambda \|\mathbf{T} \mathbf{x}\|_* \quad (5)$$

₁₅₈ Note that this step suffices in the case of single-shot EPI acquisition.

₁₅₉ II. For multi-shot EPI acquisition, shot-to-shot phase variation is extracted
₁₆₀ from \mathbf{x} . As phase images are spatially smooth ([Chen et al., 2013; Dai](#)

161 et al., 2023), only the central quarter k -space region of \mathbf{y} is used to solve
162 for \mathbf{x} . Afterward, the reconstructed \mathbf{x} is interpolated to the full FOV.
163 The corresponding phase is then filtered by the Hanning window.

164 III. Joint reconstruction of all DW images using the shot-combined forward
165 model \mathbf{E}_2 with shot-to-shot phase variation from Step II:

$$\operatorname{argmin}_{\tilde{\mathbf{x}}} \|\mathbf{y} - \mathbf{E}_2 \tilde{\mathbf{x}}\|_2^2 + \lambda \|\mathbf{T} \tilde{\mathbf{x}}\|_* \quad (6)$$

166 2.5. Locally low rank (LLR) regularization

167 As shown in Fig. 1 (D), low rankness exists in local patches from multi-
168 shell DW images. Intuitively, low rankness comes from the contrast variation
169 feature of DW images. This motivates the application of LLR regularization
170 (Trzasko and Manduca, 2011; Zhang et al., 2015) for solving the inverse
171 problems in Eqs. (5) and (6). Here, λ is the regularization strength ($\lambda \geq 0$).
172 \mathbf{T} represents a linear operator that firstly slides a local patch window through
173 all DW images and then flattens every set of local patches to two-dimensional
174 (2D) matrices. The nuclear norm regularization is enforced via singular value
175 thresholding of all flattened 2D matrices (Cai et al., 2010). We implemented
176 this regularization term as an proximal operator (Beck, 2017).

177 Noteworthy, it has been reported that LLR is prone to checkerboard
178 artifacts when λ is too large (Hu et al., 2020). We overcome this problem
179 utilizing overlapping blocks and provide an efficient implementation. If the
180 blocks overlap, $\mathbf{T}^H \mathbf{T}$ input \neq input, where \mathbf{T}^H denotes the adjoint operator
181 of \mathbf{T} . Our efficient implementation is to scale \mathbf{T}^H as $(1/\text{divisor})\mathbf{T}^H$, where
182 the divisor matrix is obtained by $\mathbf{T}^H \mathbf{T} \mathbf{1}$. $\mathbf{1}$ denotes the matrix of ones with
183 the same shape as input.

184 2.6. Reconstruction

185 The acquired raw data was read in by twixtools (<https://github.com/pehses/twixtools>). Ramp-sampling regridding and FOV/2-ghost correction were also performed in twixtools. Subsequently, coil sensitivity maps were computed from reference scans using ESPIRiT (Uecker et al., 2014) in SigPy (Ong and Lustig, 2019).

190 With this pre-processing as well as the implemented forward models and
191 the proximal operator, both inverse problems in Eqs. (5) and (6) were solved
192 by the alternating direction method of multipliers (ADMM) (Boyd et al.,
193 2010).

194 ADMM solves the minimization problems in an alternating update scheme,

$$\begin{cases} \mathbf{x}^{(k+1)} := \underset{\mathbf{x}}{\operatorname{argmin}} \| \mathbf{y} - \mathbf{E}(\mathbf{x}) \|^2 + \rho/2 \| \mathbf{T}\mathbf{x} - \mathbf{z}^{(k)} + \mathbf{u}^{(k)} \|_2^2 \\ \mathbf{z}^{(k+1)} := \mathcal{T}_{\lambda/\rho}(\mathbf{T}\mathbf{x}^{(k+1)} + \mathbf{u}^{(k)}) \\ \mathbf{u}^{(k+1)} := \mathbf{u}^{(k)} + \mathbf{T}\mathbf{x}^{(k+1)} - \mathbf{z}^{(k+1)} \end{cases} \quad (7)$$

195 where k denotes the ADMM iteration. \mathbf{z} is the auxiliary variable ($\mathbf{z} = \mathbf{T}\mathbf{x}$),
196 and \mathbf{u} is the Lagrangian multipliers. Noteworthy, in Eq. (7), \mathbf{x} \mathbf{E} stand
197 for shot images and \mathbf{E}_1 when solving Eq. (2), and shot-combined images
198 and \mathbf{E}_2 when solving Eq. (4), respectively. \mathbf{x} can be solved using linear least
199 square algorithms, e.g. conjugate gradient (Hestenes and Stiefel, 1952), while
200 \mathbf{z} is updated via singular value thresholding. The coupling parameter ρ is
201 effective in both the update of \mathbf{x} and \mathbf{z} . It acts as Tikhonov regularization
202 strength when updating \mathbf{x} , but also inversely scales the thresholding strength
203 when updating \mathbf{z} , ss shown in Supporting Information Figures S1 and S2.

204 In this work, 15 ADMM iterations with $\rho = 0.05$ and $\lambda = 0.04$, and a
205 block size of 6 for LLR (refer to Supporting Information Figure S3) were

206 used. All reconstructions were done on a single A100 SXM4/Nvlink GPU
207 with 40 GB memory (NVIDIA, Santa Clara, CA, USA).

208 We compared our proposed joint reconstruction with established multi-
209 shot reconstruction techniques, i.e. MUSE (Chen et al., 2013) and MUSSELS
210 (Mani et al., 2017). We implemented both techniques in Python and vali-
211 dated them with open-source codes and data (Dai et al., 2023; Bilgic et al.,
212 2019). For implementation details, please refer to "Reproducing MUSE
213 and MUSSELS in Python" in the Supporting Information. Further, we de-
214 noised MUSE diffusion-weighted images with local PCA (Manjón et al., 2013;
215 Veraart et al., 2016).

216 With reconstructed DW images, fractional anisotropy (FA) maps (Basser
217 et al., 1994) were fitted using our implementation in Python, whereas fiber
218 orientation distribution functions (fODF) (Aganj et al., 2009) were computed
219 in MITK-Diffusion (Fritzsche et al., 2012) with the spherical harmonic order
220 4 and the regularization factor 0.002. fODF maps were displayed with the
221 min-max normalization and the FA/GFA scaling factor 2.2.

222 **3. Results**

223 *3.1. Single-shell diffusion acquisition at 1.2 mm isotropic resolution*

224 Fig. 2 displays a DW image for one diffusion direction and zoomed-in
225 colored FA maps from MUSE, MUSE with denoising, MUSSELS, and JETS
226 reconstruction. Both MUSE and MUSSELS exhibit residual noise artifacts
227 for the single-shell acquisition with the b -value of 1000 s/mm². The local PCA
228 denoiser removes noise, but the denoised DW image loses fine structures,
229 e.g. the cuneus (highlighted by the arrows in the figure). This over-smoothing
230 effect can also be observed in the colored FA map, where the thin fibers near
231 to gray matter are missing.

232 *3.2. Three-shell diffusion acquisition at 1.0 mm isotropic resolution*

233 Results for a 1.0 mm isotropic resolution three-shell 126-direction diffusion
234 acquisition are shown in Fig. 3. At this resolution severe reduction of signal-
235 to-noise ratio (SNR) can be observed for higher b -values. With such low SNR
236 levels, brain structures are completely buried below the noise level in MUSE
237 and MUSSELS. The local PCA denoiser removes noise efficiently from the
238 reconstructed MUSE images, but images from higher b -values suffer from
239 severe blurring that leads to a loss of fine image details. Only the proposed
240 JETS method with the combination of the k_y -shift encoding scheme and LLR
241 regularized reconstruction allows to resolve brain features for higher b -values.

242 Fig. 4 shows fitted FA maps in three orthogonal orientations based on
243 the above four DW image reconstruction methods. Corresponding color-
244 coded FA maps are provided in Supporting Information Figure S6. All FA
245 maps are displayed with the same windowing, i.e., minimal and maximal

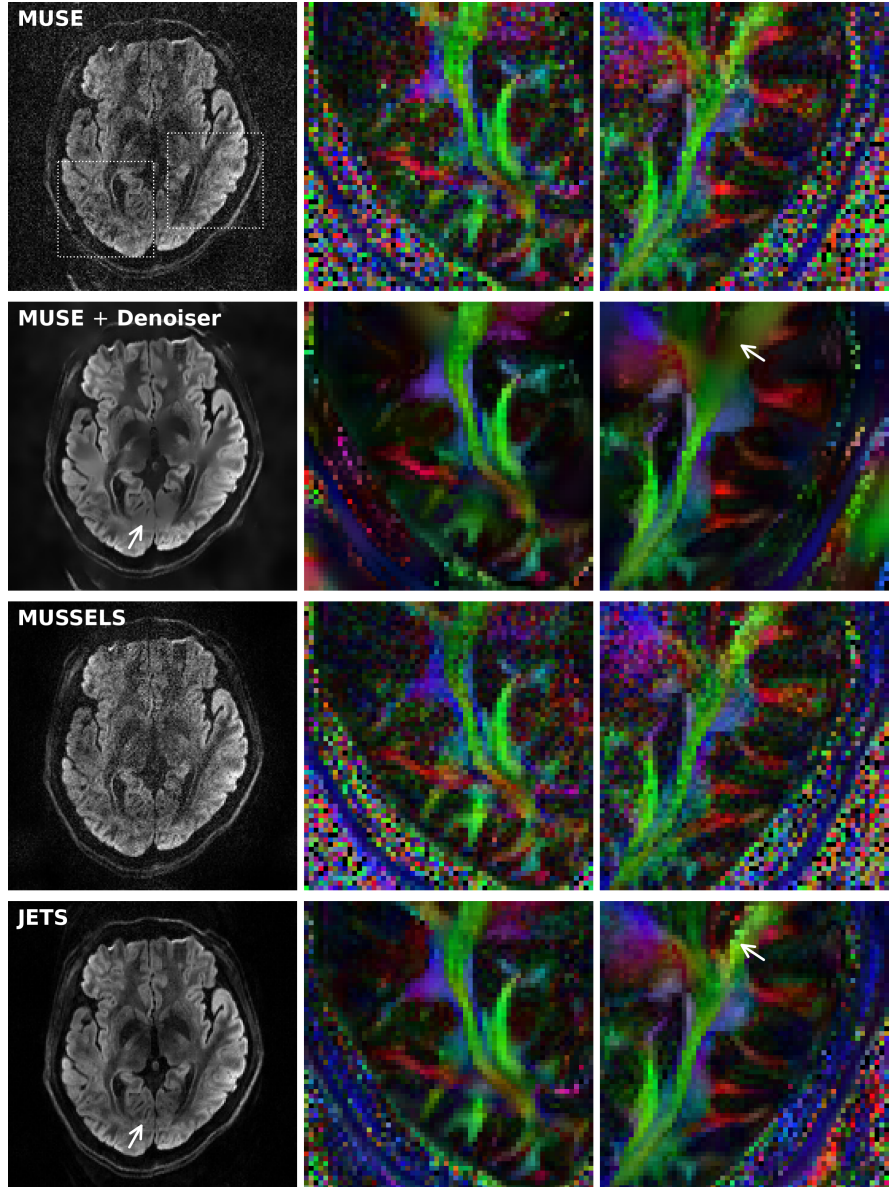


Figure 2: Comparison of reconstructions of a single-shell diffusion acquisition at 1.2 mm isotropic resolution: (1st row) MUSE, (2nd row) MUSE with local PCA denoising, (3rd row) MUSSELS, and (4th row) our proposed JETS approach. The DW image of the 42nd slice and 24th diffusion direction and its zoomed-in colored fractional anisotropy (FA) maps (dashed rectangles) are displayed. The denoiser over-smoothes the images, resulting in missing thin veins and fibers (indicated by yellow arrows).

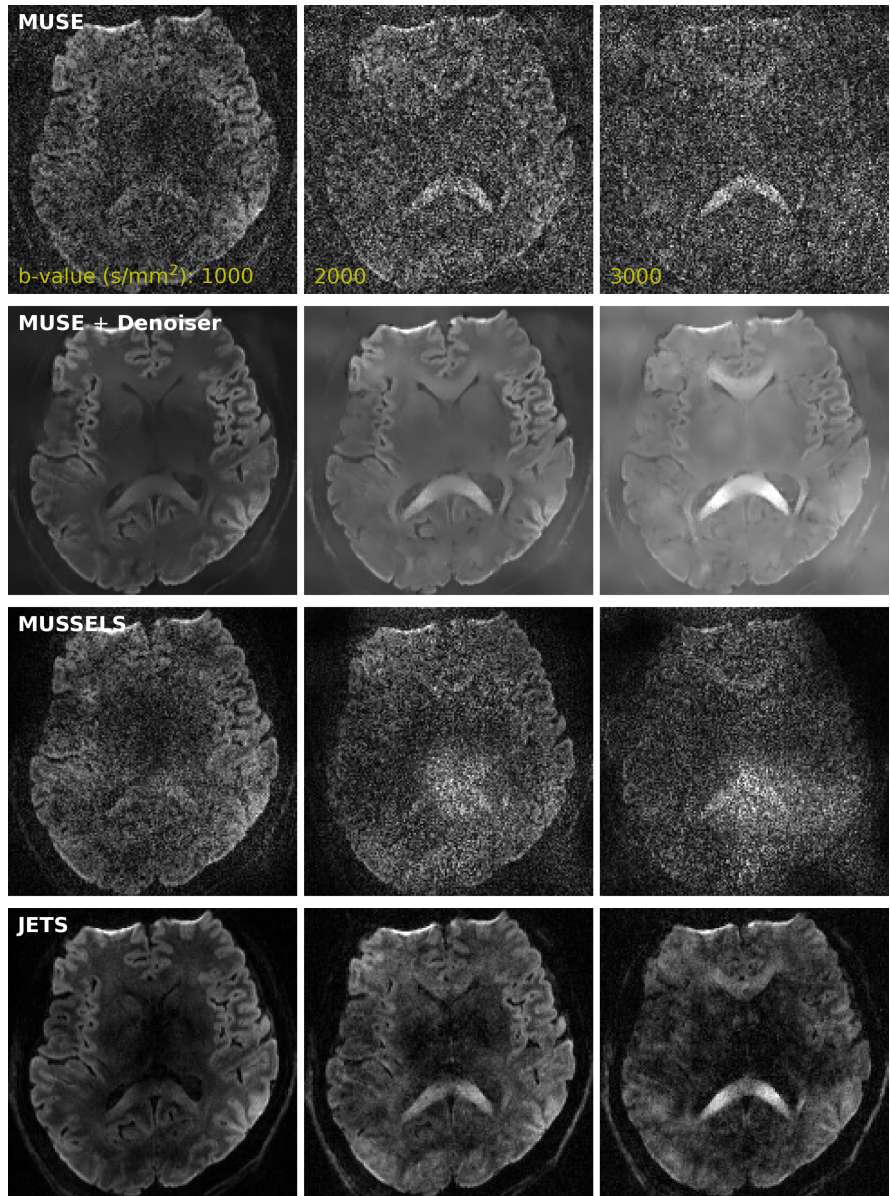


Figure 3: Comparison of reconstructed DW images on three-shell diffusion acquisition at 1 mm isotropic resolution. DW images of the 60th slice for one diffusion direction at different b -values are displayed: (left) 1000, (center) 2000, and (right) 3000 s/mm^2 .

values set as 0 and 1, respectively. The FA maps from MUSE with local PCA denoising exhibit much lower values than other methods. This may be caused by the excessive noise in DW images from MUSE or by the automatic noise estimate in the local PCA denoising algorithm (Veraart et al., 2016). Among all methods, FA maps from JETS show better quality and delineate fine details within the putamen (see white arrows).

Fig. 5 shows fODF maps within the rectangular regions in Fig. 4. This result again demonstrates the advantage of iterative reconstruction with LLR regularization for DW image denoising. Both MUSE and MUSSELS reconstructions suffer from noise artifacts due to the use of highly accelerated acquisition ($R = 8.7 \times 3$ per shot) and high b -values (up to 3000 s/mm^2). As a result, their corresponding fODF maps illustrate chaotic fiber orientation. With the local PCA denoiser applied to DW images reconstructed by MUSE, the fODF peaks show improved smooth patterns, but the FA values are reduced due to excessive noise in DW images. In contrast, with LLR regularization applied to the spatial-angular patches, JETS is able to resolve crossing fibers in the intersection of corpus callosum and superior longitudinal fasciculus (see white arrows).

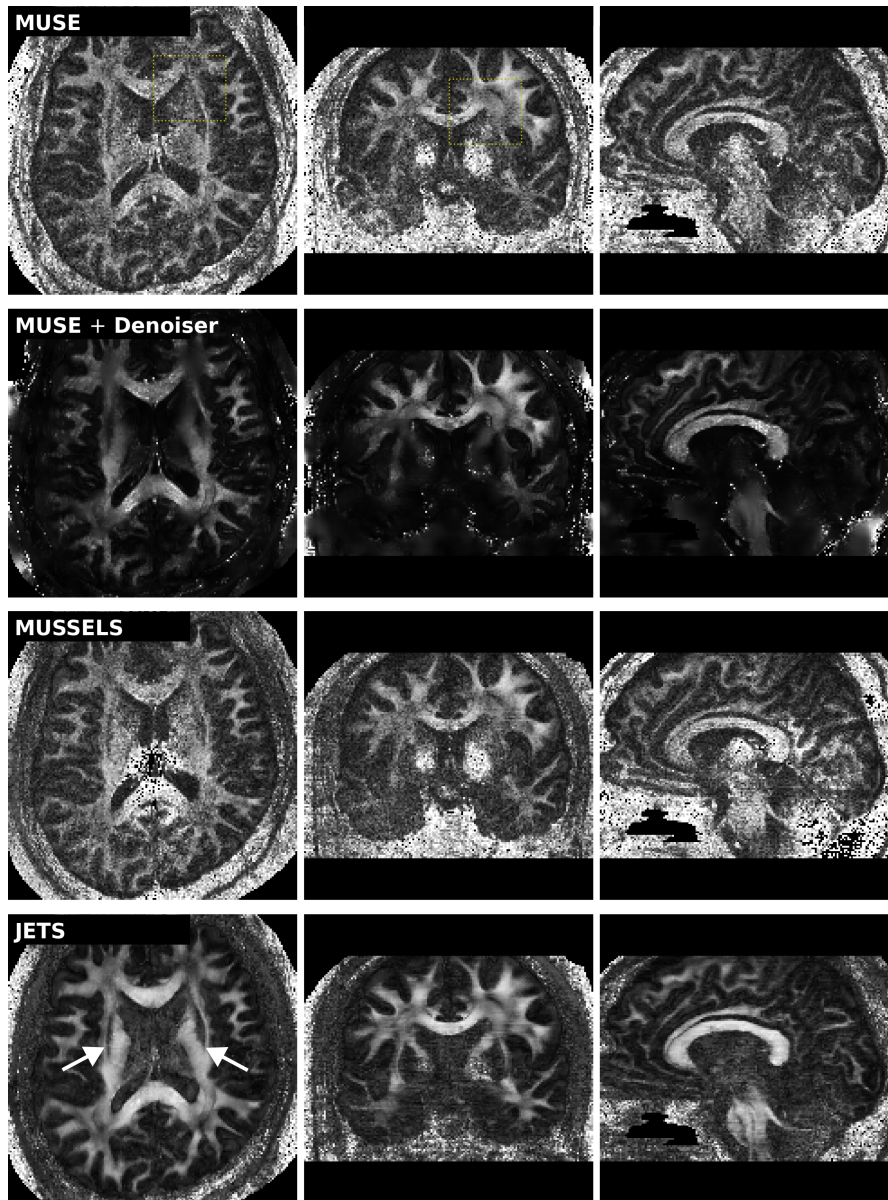


Figure 4: Comparison of reconstructed FA maps based on the 1 mm isotropic resolution three-shell diffusion acquisition. One slice from every orientation (axial, coronal, and sagittal view from left to right) was selected for display.

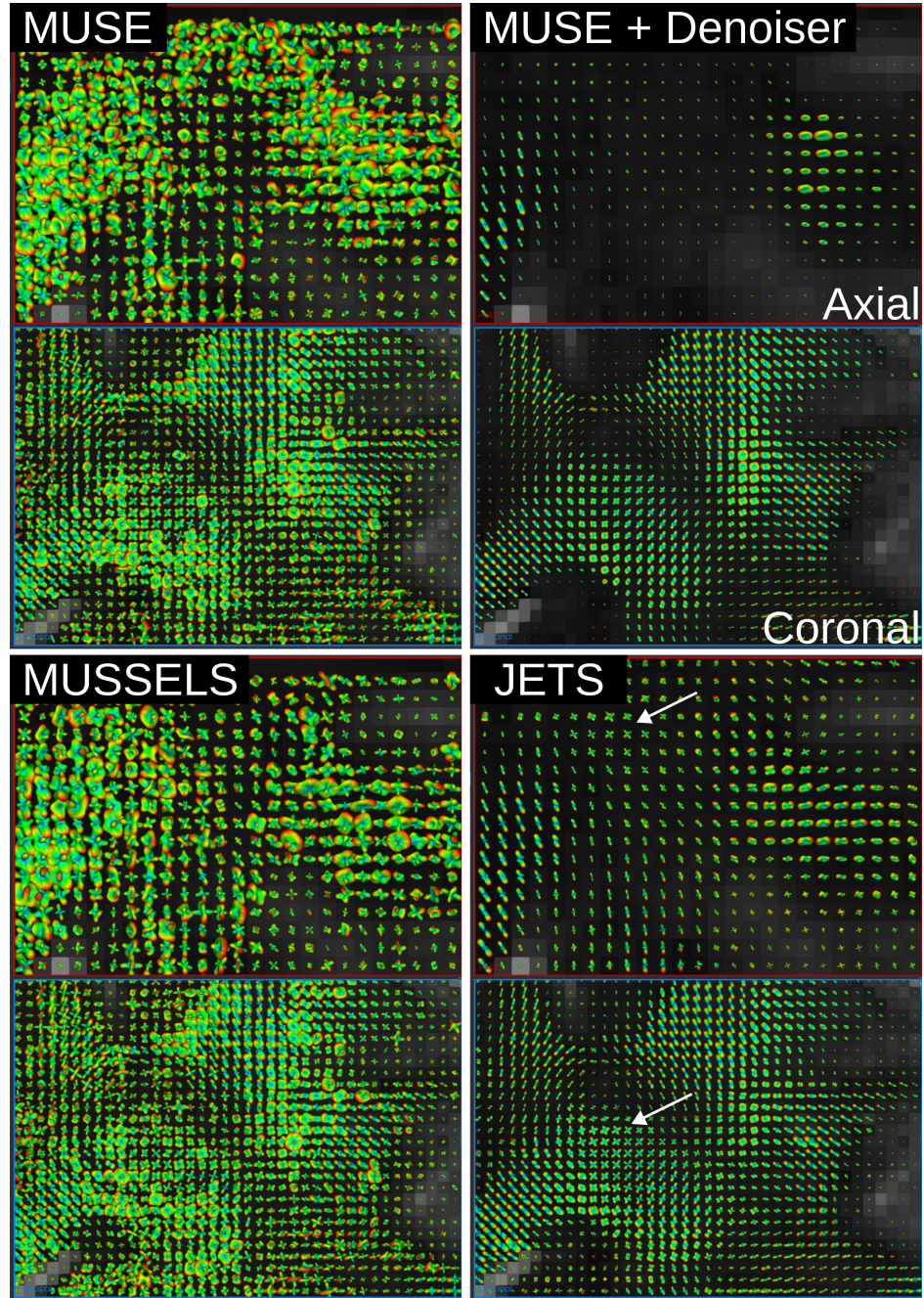


Figure 5: Comparison of fODF peaks within the dashed rectangles of (red) the axial and (blue) the coronal slices in Fig. 4, respectively.

264 **4. Discussion**

265 This work reports a novel DW-MRI technique, dubbed as JETS-EPI,
266 comprising two ingredients, multi-band k_y -shift-encoded interleaved EPI for
267 complementary k - q -space sampling, and a generalized joint reconstruction
268 with overlapping locally low-rank regularization to explore low rankness along
269 the diffusion encoding dimension. JETS-EPI utilizes only two shots per
270 diffusion direction, thereby allowing for short scan time as well as high spatial
271 resolution with reduced geometric distortion. Our reconstruction achieves
272 8.7×3 ($R_{\text{inplane}} \times \text{SMS}$) fold accelerated brain DW-MRI at 7 T with 1 mm
273 isotropic resolution and 126 diffusion-direction (three shells with b -values of
274 1000, 2000, and 3000 s/mm²) in less than 23 min.

275 The reconstruction results from MUSE and MUSSELS suffer from noise
276 effects in this study, and the reasons are two-fold. First, the high in-plane
277 acceleration factor per shot hinders shot-to-shot phase variation estimation
278 in MUSE, whereas we proposed to jointly reconstruct all shot images from
279 the central k -space data. Further, joint reconstruction benefits from the
280 complementary k - q -space sampling, as compared to the shot-by-shot parallel
281 imaging reconstruction. Second, structured low-rank matrix completion as
282 MUSSELS usually works with at least four shots per diffusion direction,
283 whereas this study uses only two shots. The use of two shots is beneficial
284 for shorter scan time than four shots, but hinders the structured low rank
285 property in MUSSELS.

286 One limitation of JETS-EPI is the long reconstruction time due to the
287 simultaneous reconstruction of all DW images and the use of overlapping
288 locally low-rank regularization. The reconstruction of the protocols in Sec-

tion 2.2.1 and Section 2.2.2 on GPU A100 takes about 0.5 h and 3 h per collapsed slice, respectively. To reduce the computation time, coil compression algorithms (Huang et al., 2008) can be employed to reduce the number of coils for image reconstruction. Moreover, one may deploy multi-GPU distributed computing or modern optimization algorithms (e.g. stochastic gradient descent) (Ong et al., 2020) to speed up the reconstruction.

Another limitation of JETS-EPI is the self-navigated shot-to-shot phase variation estimation, which was performed based on the central quarter k -space region of every shot. These shot k -space data is highly undersampled with $R = 8.7 \times 3$ for the 1 mm three-shell diffusion acquisition. Such high acceleration may result in sub-optimal phase estimation, especially in regions with low SNR and/or rapid phase change.

While this work reconstructs all DW images and then performs model fitting, an alternative approach is to directly estimate b_0 and diffusion tensors from measured k - q -space data using model-based reconstruction (Knoll et al., 2015; Dong et al., 2018; Shafieizargar et al., 2023). Compared to DW image reconstruction, model-based reconstruction solves for fewer number of unknowns, but requires strict diffusion tensor modeling and the use of nonlinear least square solvers.

5. Conclusions

We demonstrated the JETS-EPI technique, which integrates a k_y -shifted encoding interleaved EPI sequence and a joint reconstruction with overlapping locally low-rank regularization for high spatial-angular-temporal resolution DW-MRI at 7 T. This technique requires no phase navigation, and

313 allows for high quality DW image reconstruction with accelerated acquisition.
314

315 **Funding**

316 This work was supported by Deutsche Forschungsgemeinschaft (DFG) -
317 Project Number 513220538, as well as National Institutes of Health (NIH)
318 R01 EB024532 and P41 EB017183.

319 **Data and code available statement**

320 In the spirit of reproducible and open science, we will publish our source
321 code (<https://github.com/ZhengguoTan/sigpy>) as well as the raw k -space
322 data (<https://doi.org/10.5281/zenodo.7548595>) during the review pro-
323 cess.

324 **Acknowledgments**

325 The authors thank Dr. Peter Neher for discussions. The authors grate-
326 fully acknowledge the scientific support and HPC resources provided by the
327 Erlangen National High Performance Computing Center (NHR@FAU) of
328 Friedrich-Alexander-Universität Erlangen-Nürnberg (FAU) under the NHR
329 project b143dc. NHR funding is provided by federal and Bavarian state au-
330 thorities. NHR@FAU hardware is partially funded by the German Research
331 Foundation (DFG) – 440719683.

332 **References**

- 333 Aganj, I., Lenglet, C., Sapiro, G., 2009. Odf reconstruction in q-ball imaging with solid angle consideration, in: Proc. IEEE Int. Symp. Biomed. Imaging, pp. 1398–1401. doi:[10.1109/ISBI.2009.5193327](https://doi.org/10.1109/ISBI.2009.5193327).
- 336 Bammer, R., Keeling, S.L., Augustin, M., Pruessmann, K.P., Wolf, R., Stoll-
337 berger, R., Hartung, H.P., Fazekas, F., 2001. Improved diffusion-weighted
338 single-shot echo-planar imaging (EPI) in stroke using sensitivity encoding
339 (SENSE). Magn. Reson. Med. 46, 548–554. doi:[10.1002/mrm.1226](https://doi.org/10.1002/mrm.1226).
- 340 Basser, P.J., Mattiello, J., Le Bihan, D., 1994. MR diffusion tensor
341 spectroscopy and imaging. Biophys. J. 66, 259–267. doi:[10.1016/S0006-3495\(94\)80775-1](https://doi.org/10.1016/S0006-3495(94)80775-1).
- 343 Beck, A., 2017. First-order methods in optimization. Society for In-
344 dustrial and Applied Mathematics, Philadelphia, PA. doi:[10.1137/1.9781611974997](https://doi.org/10.1137/1.9781611974997).
- 346 Bilgic, B., Chatnuntawech, I., Manhard, M.K., Tian, Q., Liao, C., Iyer, S.S.,
347 Cauley, S.F., Huang, S.Y., Polimeni, J.R., Wald, L.L., Setsompop, K.,
348 2019. Highly accelerated multishot echo planar imaging through synergistic
349 machine learning and joint reconstruction. Magn. Reson. Med. 82, 1343–
350 1358. doi:[10.1002/mrm.27813](https://doi.org/10.1002/mrm.27813).
- 351 Block, K.T., Uecker, M., Frahm, J., 2007. Undersampled radial MRI with
352 multiple coils. Iterative image reconstruction using a total variation con-
353 straint. Magn. Reson. Med. 57, 1186–1098. doi:[10.1002/mrm.21236](https://doi.org/10.1002/mrm.21236).

- 354 Boyd, S., Parikh, N., Chu, E., Peleato, B., Eckstein, J., 2010. Distributed
355 optimization and statistical learning via the alternating direction method
356 of multipliers. *Foundations and Trends in Machine Learning* 3, 1–122.
357 doi:[10.1561/2200000016](https://doi.org/10.1561/2200000016).
- 358 Breuer, F.A., Blaimer, M., Heidemann, R.M., Mueller, M.F., Griswold, M.A.,
359 Jakob, P.M., 2005. Controlled Aliasing in Parallel Imaging Results in
360 Higher Acceleration (CAPIRINHA) for Multi-Slice Imaging. *Magn. Reson.*
361 *Med.* 53, 684–691. doi:[10.1002/mrm.20401](https://doi.org/10.1002/mrm.20401).
- 362 Butts, K., Riederer, S.J., Ehman, R.L., Thompson, R.M., Jack, C.R., 1993.
363 Interleaved echo planar imaging on a standard MRI system. *Magn. Reson.*
364 *Med.* 31, 67–72. doi:[10.1002/mrm.1910310111](https://doi.org/10.1002/mrm.1910310111).
- 365 Cai, J.F., Candès, E.J., Shen, Z., 2010. A singular value thresholding
366 algorithm for matrix completion. *SIAM. J. Optim.* 20, 1956–1982.
367 doi:[10.1137/080738970](https://doi.org/10.1137/080738970).
- 368 Chen, N.K., Guidon, A., Chang, H.C., Song, A.W., 2013. A robust multi-
369 shot scan strategy for high-resolution diffusion weighted MRI enabled by
370 multiplexed sensitivity-encoding (MUSE). *NeuroImage* 72, 41–47. doi:[10.1016/j.neuroimage.2013.01.038](https://doi.org/10.1016/j.neuroimage.2013.01.038).
- 372 Dai, E., Mani, M., McNab, J.A., 2023. Multi-band multi-shot diffu-
373 sion MRI reconstruction with joint usage of structured low-rank con-
374 straints and explicit phase mapping. *Magn. Reson. Med.* 89, 95–111.
375 doi:[10.1002/mrm.29422](https://doi.org/10.1002/mrm.29422).

- 376 Dong, Z., Dai, E., Wang, F., Zhang, Z., Ma, X., Yuan, C., Guo, H., 2018.
377 Model-based reconstruction for simultaneous multislice and parallel imag-
378 ing accelerated multishot diffusion tensor imaging. *Med. Phys.* 45, 3196–
379 3204. doi:[10.1002/mp.12974](https://doi.org/10.1002/mp.12974).
- 380 Fritzzsche, K.H., Neher, P.F., Reicht, I., van Bruggen, T., Goch, C., Reisert,
381 M., Nolden, M., Zelzer, S., Meinzer, H.P., Stieltjes, B., 2012. MITK diffu-
382 sion imaging. *Methods Inf. Med.* 51, 441–448. doi:[10.3414/ME11-02-0031](https://doi.org/10.3414/ME11-02-0031).
- 383 Griswold, M.A., Jakob, P.M., Heidemann, R.M., Nittka, M., Jellus, V.,
384 Wang, J., Kiefer, B., Haase, A., 2002. Generalized autocalibrating par-
385 tially parallel acquisitions (GRAPPA). *Magn. Reson. Med.* 47, 1202–1210.
386 doi:[10.1002/mrm.10171](https://doi.org/10.1002/mrm.10171).
- 387 Guhaniyogi, S., Chu, M.L., Chang, H.C., Song, A.W., Chen, N.K., 2016. Mo-
388 tion immune diffusion imaging using augmented MUSE for high-resolution
389 multi-shot EPI. *Magn. Reson. Med.* 75, 639–652. doi:[10.1002/mrm.25624](https://doi.org/10.1002/mrm.25624).
- 390 Heidemann, R.M., Porter, D.A., Anwander, A., Feiweier, T., Heberlein, K.,
391 Knösche, T.R., Turner, R., 2010. Diffusion imaging in humans at 7 T
392 using readout-segmented EPI and GRAPPA. *Magn. Reson. Med.* 64, 9–
393 14. doi:[10.1002/mrm.22480](https://doi.org/10.1002/mrm.22480).
- 394 Hestenes, M.R., Stiefel, E., 1952. Methods of conjugate gradients for solving
395 linear systems. *J. Res. Natl. Bur. Stand.* 49, 409–436. doi:[10.6028/jres.049.044](https://doi.org/10.6028/jres.049.044).
- 397 Hu, Y., Wang, X., Tian, Q., Yang, G., Daniel, B., McNab, J., Hargreaves, B.,
398 2020. Multi-shot diffusion-weighted MRI reconstruction with magnitude-

- 399 based spatial-angular locally low-rank regularization (SPA-LLR). Magn.
400 Reson. Med. 83, 1596–1607. doi:[10.1002/mrm.28025](https://doi.org/10.1002/mrm.28025).
- 401 Huang, F., Vijayakumar, S., Li, Y., Hertel, S., Duensing, G.R., 2008. A soft-
402 ware channel compression technique for faster reconstruction with many
403 channels. Magn. Reson. Imaging 26, 133–141.
- 404 Jones, D.K., 2010. Diffusion MRI: Theory, methods, and applications. Oxford
405 University Press.
- 406 Knoll, F., Raya, J.G., Halloran, R.O., Baete, S., Sigmund, E., Bammer, R.,
407 Block, T., Otazo, R., Sodickson, D.K., 2015. A model-based reconstruction
408 for undersampled radial spin-echo DTI with variational penalties on the
409 diffusion tensor. NMR Biomed 28, 353–366.
- 410 Le Bihan, D., Breton, E., Lallemand, D., Grenier, P., Cabanis, E., Laval-
411 Jeantet, M., 1986. MR imaging of intravoxel incoherent motions: appli-
412 cation to diffusion and perfusion in neurologic disorders. Radiology 161,
413 401–407. doi:[10.1148/radiology.161.2.3763909](https://doi.org/10.1148/radiology.161.2.3763909).
- 414 Liu, C., Moseley, M.E., Bammer, R., 2005. Simultaneous phase cor-
415 rection and SENSE reconstruction for navigated multi-shot DWI with
416 non-Cartesian k -space sampling. Magn. Reson. Med. 54, 1412–1422.
417 doi:[10.1002/mrm.20706](https://doi.org/10.1002/mrm.20706).
- 418 Lustig, M., Donoho, D., Pauly, J.M., 2007. Sparse MRI: The application of
419 compressed sensing for rapid MR imaging. Magn. Reson. Med. 58, 1182–
420 1195. doi:[10.1002/mrm.21391](https://doi.org/10.1002/mrm.21391).

- 421 Mani, M., Jacob, M., Kelley, D., Magnotta, V., 2017. Multi-shot sensitivity-
422 encoded diffusion data recovery using structured low-rank matrix comple-
423 tion (MUSSELS). *Magn. Reson. Med.* 78, 494–507. doi:[10.1002/mrm.26382](https://doi.org/10.1002/mrm.26382).
- 425 Manjón, J.V., Coupé, P., Concha, L., Buades, A., Collins, D.L., Robles, M.,
426 2013. Diffusion weighted image denoising using overcomplete local PCA.
427 *PLoS One* 8, e73021. doi:[10.1371/journal.pone.0073021](https://doi.org/10.1371/journal.pone.0073021).
- 428 Mansfield, P., 1977. Multi-planar image formation using NMR spin echoes.
429 *J Phys C* 10, 55–58. doi:[10.1088/0022-3719/10/3/004](https://doi.org/10.1088/0022-3719/10/3/004).
- 430 Maudsley, A.A., 1980. Multiple-line-scanning spin density imaging. *J. Magn.*
431 *Reson.* 41, 112–126. doi:[10.1016/0022-2364\(80\)90207-3](https://doi.org/10.1016/0022-2364(80)90207-3).
- 432 Merboldt, K.D., Hanicke, W., Frahm, J., 1985. Self-diffusion NMR imag-
433 ing using stimulated echoes. *J. Magn. Reson.* 64, 479–486. doi:[10.1016/0022-2364\(85\)90111-8](https://doi.org/10.1016/0022-2364(85)90111-8).
- 435 Mori, S., Crain, B.J., Chacko, V.P., Van Zijl, P.C.M., 1999. Three-
436 dimensional tracking of axonal projections in the brain by mag-
437 netic resonance imaging. *Ann. Neurol.* 45, 265–269. doi:[10.1002/1531-8249\(199902\)45:2<265::AID-ANA21>3.0.CO;2-3](https://doi.org/10.1002/1531-8249(199902)45:2<265::AID-ANA21>3.0.CO;2-3).
- 439 Ong, F., Lustig, M., 2019. SigPy: A Python package for high performance
440 iterative reconstruction, in: Proceedings of the 27th Annual Meeting of
441 ISMRM, Montréal, CAN, p. 4819.
- 442 Ong, F., Zhu, X., Cheng, J.Y., Johnson, K.M., Larson, P.E.Z., Vasanawala,
443 S.S., Lustig, M., 2020. Extreme MRI: Large-scale volumetric dynamic

- 444 imaging from continuous non-gated acquisitions. Magn. Reson. Med. 84,
445 1763–1780. doi:[10.1002/mrm.28235](https://doi.org/10.1002/mrm.28235).
- 446 Pipe, J.G., Farthing, V.G., Forbes, K.P., 2002. Multishot diffusion-weighted
447 FSE using PROPELLER MRI. Magn. Reson. Med. 47, 42–52. doi:[10.1002/mrm.10014](https://doi.org/10.1002/mrm.10014).
- 449 Porter, D.A., Heidemann, R.M., 2009. High resolution diffusion-weighted
450 imaging using readout-segmented echo-planar imaging, parallel imaging
451 and a two-dimensional navigator-based reacquisition. Magn. Reson. Med.
452 62, 468–475. doi:[10.1002/mrm.22024](https://doi.org/10.1002/mrm.22024).
- 453 Pruessmann, K.P., Weiger, M., Scheidegger, M.B., Boesiger, P., 1999.
454 SENSE: Sensitivity encoding for fast MRI. Magn. Reson. Med. 42, 952–
455 962. doi:[10.1002/\(SICI\)1522-2594\(199911\)42:5<952::AID-MRM16>3.0.CO;2-S](https://doi.org/10.1002/(SICI)1522-2594(199911)42:5<952::AID-MRM16>3.0.CO;2-S).
- 457 Ra, J.B., Rim, C.Y., 1993. Fast imaging using subencoding data sets from
458 multiple detectors. Magn. Reson. Med. 30, 142–145. doi:[10.1002/mrm.1910300123](https://doi.org/10.1002/mrm.1910300123).
- 460 Roemer, P.B., Edelstein, W.A., Hayes, C.E., Souza, S.P., Mueller, O.M.,
461 1990. The NMR phased array. Magn. Reson. Med. 16, 192–225. doi:[10.1002/mrm.1910160203](https://doi.org/10.1002/mrm.1910160203).
- 463 Shafieizargar, B., Jeurissen, B., Poot, D.H.J., Klein, S., Van Audekerke,
464 J., Verhoye, M., den Dekker, A.J., Sijbers, J., 2023. ADEPT: Accurate
465 diffusion echo-planar imaging with multi-contrast sh0Ts. Magn. Reson.
466 Med. 89, 396–410. doi:[10.1002/mrm.29398](https://doi.org/10.1002/mrm.29398).

- ⁴⁶⁷ Truong, T.K., Guidon, A., 2014. High-resolution multishot spiral diffusion
⁴⁶⁸ tensor imaging with inherent correction of motion-induced phase errors.
⁴⁶⁹ Magn. Reson. Med. 71, 790–796. doi:[10.1002/mrm.24709](https://doi.org/10.1002/mrm.24709).
- ⁴⁷⁰ Trzasko, J., Manduca, A., 2011. Local versus global low-rank promotion in
⁴⁷¹ dynamic MRI series reconstruction, in: Proceedings of the 19th Annual
⁴⁷² Meeting of ISMRM, Montréal, CAN, p. 4371.
- ⁴⁷³ Tuch, D.S., Reese, T.G., Wiegell, M.R., Makris, N., Belliveau, J.W., Wedeen,
⁴⁷⁴ V.J., 2002. High angular resolution diffusion imaging reveals intravoxel
⁴⁷⁵ white matter fiber heterogeneity. Magn. Reson. Med. 48, 577–582. doi:[10.1002/mrm.10268](https://doi.org/10.1002/mrm.10268).
- ⁴⁷⁷ Uecker, M., Lai, P., Murphy, M.J., Virtue, P., Elad, M., Pauly, J.M.,
⁴⁷⁸ Vasanawala, S.S., Lustig, M., 2014. ESPIRiT – an eigenvalue approach
⁴⁷⁹ to autocalibrating parallel MRI: Where SENSE meets GRAPPA. Magn.
⁴⁸⁰ Reson. Med. 71, 990–1001. doi:[10.1002/mrm.24751](https://doi.org/10.1002/mrm.24751).
- ⁴⁸¹ Veraart, J., Novikov, D.S., Christiaens, D., Ades-aron, B., Sijbers, J., Fiere-
⁴⁸² mans, E., 2016. Denoising of diffusion mri using random matrix theory.
⁴⁸³ NeuroImage 142, 394–406. doi:[10.1016/j.neuroimage.2016.08.016](https://doi.org/10.1016/j.neuroimage.2016.08.016).
- ⁴⁸⁴ Wu, W., Koopmans, P.J., Andersson, J.L., Miller, K.L., 2019. Diffusion
⁴⁸⁵ Acceleration with Gaussian process Estimated Reconstruction (DAGER).
⁴⁸⁶ Magn. Reson. Med. 82, 107–125. doi:[10.1002/mrm.27699](https://doi.org/10.1002/mrm.27699).
- ⁴⁸⁷ Zhang, T., Pauly, J.M., Levesque, I.R., 2015. Accelerated parameter mapping
⁴⁸⁸ with a locally low rank constraint. Magn. Reson. Med. 73, 655–661. doi:[10.1002/mrm.25161](https://doi.org/10.1002/mrm.25161).